

THREE-DIMENSIONAL SIMULATIONS OF DISK ACCRETION TO AN INCLINED DIPOLE. II. HOT SPOTS AND VARIABILITY

M. M. ROMANOVA

Department of Astronomy, Cornell University, 410 Space Sciences Building, Ithaca, NY 14853-6801; romanova@astro.cornell.edu

G. V. USTYUGOVA

Keldysh Institute of Applied Mathematics, Russian Academy of Sciences, 4 Miuskaya Square, Moscow 125047, Russia; ustyugg@spp.keldysh.ru

A. V. KOLDOBA

Institute of Mathematical Modeling, Russian Academy of Sciences, 4 Miuskaya Square, Moscow 125047, Russia; koldoba@spp.keldysh.ru

AND

R. V. E. LOVELACE

Department of Astronomy, Cornell University, 412 Space Sciences Building, Ithaca, NY 14853-6801; rv11@cornell.edu

Received 2004 January 12; accepted 2004 April 6

ABSTRACT

The physics of the hot spots on stellar surfaces and the associated variability of accreting magnetized rotating stars is investigated for the first time using fully three-dimensional magnetohydrodynamic simulations. The magnetic moment of the star, μ , is inclined relative to its rotation axis, Ω , by an angle Θ (we call this angle the “misalignment angle”), while the disk’s rotation axis is parallel to Ω . A sequence of misalignment angles between $\Theta = 0^\circ$ and 90° was investigated. The hot spots arise on the stellar surface because of the impact on the surface of magnetically channeled accretion streams. The distribution of different parameters in the hot spots reflects those in the funnel streams near the surface of the star. Typically, at small Θ the spots as observed are shaped like a bow curved around the magnetic axis, while at the largest values of Θ the spots are shaped like a bar crossing the magnetic pole. The physical parameters (density, velocity, temperature, matter, energy fluxes, etc.) increase toward the central regions of the spots; thus, the size of the spots is different at different values of these parameters. At relatively low density and temperature, the spots occupy approximately 10%–20% of the stellar surface, while at the highest values of these parameters this area may be less than 1% of the area of the star. The size of the spots increases with the accretion rate. Rotation of the star leads to the observed variability of brightness. The light curves were calculated for different values of Θ and inclination angles of the disk, i . They show a range of variability patterns, including curves with one maximum per period (at most angles Θ and i) and curves with two maxima per period (at large Θ and i). At small Θ , the funnel streams may rotate faster or slower than the star, and this may lead to quasi-periodic variability of the star. The results are of interest for understanding the variability and quasi variability of classical T Tauri stars, millisecond pulsars, and cataclysmic variables.

Subject headings: accretion, accretion disks — magnetic fields — MHD — plasmas — stars: magnetic fields — X-rays: stars

1. INTRODUCTION

In accreting magnetized stars the inflowing matter is channeled to regions near the magnetic poles of the star, forming hot spots on the star’s surface (e.g., Ghosh & Lamb 1979; Camenzind 1990; Königl 1991; Shu et al. 1994; Hartmann et al. 1994; Hartmann 1998). The hot spots form under conditions in which the star’s magnetic field is strong enough to form a magnetosphere. Examples include classical T Tauri stars (CTTSs; e.g., Herbst et al. 1986; Bouvier & Bertout 1989; Johns & Basri 1995, 1998; Petrov et al. 2001a, 2001b; Alencar & Batalha 2002), cataclysmic variables (e.g., Wickramasinghe et al. 1991; Livio & Pringle 1992; Warner 1995, 2000), X-ray pulsars (e.g., Ghosh & Lamb 1979; Trümper et al. 1986; Bildsten et al. 1997), and millisecond pulsars (e.g., Chakrabarty et al. 2003). These objects have different dimensions and magnetic field strengths, but the underlying physics of the magnetospheric accretion and hot spots’ properties is expected to be similar.

The observed variability or quasi variability of these objects can be due to a number of possible phenomena in the

magnetosphere (see, e.g., Bouvier 2003; Petrov 2003). One of the timescales may be associated with the hot spots. In spite of the large volume of observational data on the variability of these stars, relatively little is known about the properties of the hot spots.

For example, in CTTSs hot-spot radiation is associated with veiling of the continuum radiation and was analyzed for a number of CTTSs. Herbst & Koret (1988) and Bouvier et al. (1986, 1993) estimated parameters of the hot spots by assuming a model with blackbody radiation, while Calvet & Gullbring (1998), Gullbring et al. (2000), and Ardila & Basri (2000) used models of the radiation from a shock wave. They concluded that the area of the star covered by the hot spots in different CTTSs varies from 0.3% to 20% depending on the accretion rate and other factors. In all models, however, the hot spots were considered to be homogeneous, that is, of the same density and temperature. Further, some of the models did not take into account the effect of limb darkening. In addition, the shape and location of the hot spots were not known because they can be derived only from a three-dimensional analysis. Similar problems and questions appear during analysis of

X-ray pulsars and cataclysmic variables. Thus, it is important to study the properties of the hot spots in greater detail. For analysis of the hot spots we use the results of our previous three-dimensional simulations (Romanova et al. 2003, hereafter R03) and also perform new simulations at a lower temperature in the disk and at a variety of parameters of the star and the accretion flow.

The main questions that can be answered are (1) What are the shapes of the hot spots? (2) What is the distribution of physical parameters (density and temperature) in the spots? (3) What is the area covered by the spots at different physical parameters? (4) What are the observed light curves at different misalignment angles, Θ , and different inclination angles of the disk, i ?

In § 2 of the paper we describe the underlying model and dimensional examples for CTTSs and millisecond pulsars. In § 3 we discuss the expected physical properties of the hot spots. In § 4 we calculate the intensity of radiation from the hot spots and the associated light curves. In § 5 we discuss the dependence of the results on different parameters, limitations of the model, and future work. Section 6 gives the summary of our work.

2. MODEL AND REFERENCE VALUES

Below, we briefly describe the numerical model of R03, initial and boundary conditions, and reference values for CTTSs and millisecond pulsars.

2.1. Model

Disk accretion to a rotating star with an inclined dipole magnetic field was investigated with three-dimensional MHD simulations. The magnetic moment, μ , of the dipole is inclined to the star’s rotation axis, Ω , by an angle Θ . The rotation axis of the star coincides with the rotation axis of the disk. The value of the magnetic moment, $\mu = |\mu|$, is restricted by computer resources. It is difficult to calculate in three dimensions large magnetospheres, where the magnetospheric radius, R_m , is much larger than the star’s radius, R_* . This is because of the strong variation ($\propto 1/R^3$) of the dipole magnetic field. In R03, simulations were done for $R_m/R_* \approx 2-5$. These values are appropriate for many CTTSs and millisecond pulsars. For larger magnetospheres, the inner boundary may be interpreted as an intermediate layer of magnetosphere.

A Godunov-type numerical code was used to solve the full system of ideal MHD equations in three-dimensional space written in a “cubed sphere” coordinate system rotating with the star (Koldoba et al. 2002; R03). We use a reference frame (X, Y, Z) rotating with the star. This frame is oriented such that the Z -axis is aligned with the star’s rotation axis and the vector μ is in the (X, Z) plane.

The quasi-equilibrium initial conditions were proposed and tested in an axisymmetric model by Romanova et al. (2002, hereafter R02) and in three dimensions by R03. These initial conditions take into account the initial balance of gravitational, pressure gradient, and centrifugal forces. Although this initial condition does not include the magnetic field, it avoids the possible initial discontinuity of the poloidal magnetic field lines at the boundary between the disk and corona (the corona above the disk rotates with the angular velocity of the disk). Test simulations with a nonrotating corona show strong magnetic braking and accretion of the disk with a speed close to the free-fall speed (see Hayashi et al. 1996; some runs of Miller & Stone 1997). The new initial conditions decrease this initial magnetic braking dramatically, but not completely. There is a

residual small magnetic braking that determines a slow inward accretion of matter to the star. This accretion is used as a source of accreting matter in most simulations. To check the validity of this approach, we added simplified α -type viscosity to the code, taking only the largest terms into account (as in R02), and performed a set of simulations at $\Theta = 15^\circ$ and at a variety of α -parameters (see § 5.1). Simulations have shown that the velocity of the accretion flow induced by the residual magnetic braking corresponds to that of a viscous flow with $\alpha \approx 0.01-0.02$. These initial conditions allowed us to observe for the first time the magnetospheric funnel flows from the disk to the star in two and three dimensions and to investigate them in detail (see R02; R03).

We consider the case in which the star rotates relatively slowly with angular velocity $\Omega_* \approx 0.04\Omega_{K*}$, where $\Omega_{K*} = (GM/R_*^3)^{1/2}$ is the breakup angular velocity of the star. For the case of T Tauri stars, this corresponds to a slow rotation rate ($T \approx 9.4$ days for the parameters used in R02). This rotation velocity was chosen simply because it was the main case of R03. Test cases with faster rotation of the star were also performed.

We consider two main cases: (1) a relatively hot disk where the flow to the star is subsonic and (2) a cooler disk where the flow is supersonic. The important parameters are the initial densities in the disk, ρ_d , and the corona, ρ_c , and the initial temperatures in the disk, T_d , and the corona, T_c . These values are determined at the fiducial point at the boundary between the disk and corona (at the inner radius of the disk) to support pressure balance in the vertical direction. In two-dimensional simulations (R02) we used parameters such that $\rho_c = 0.01\rho_d$ and $T_d = 0.01T_c$ and obtained supersonic funnel streams because the sound speed is relatively low, $c_s \approx 0.1v_K$. However, in three-dimensional simulations in R03 we were able to cover only a “softer” range of parameters: $\rho_c = 0.03\rho_d$ and $T_d = 0.03T_c$ when the disk has higher temperature and $c_s \approx 0.17v_K$. In this paper we use the results of R03 and newer runs with lower temperature in the disk ($c_s \approx 0.1v_K$).

The boundary conditions are similar to those in R03. At the stellar surface there are “free” boundary conditions on the density and pressure. The poloidal components of the magnetic field are determined from the fact that the star is treated as a perfect conductor rotating at the rate $\Omega = \Omega\hat{z}$. There is, however, a “free” condition on the azimuthal component of the magnetic field, $\partial(RB_\phi)/\partial R = 0$, so that magnetic field lines have “freedom” to bend near the stellar surface. In the reference frame rotating with the star the flow velocity is adjusted to be parallel to \mathbf{B} at $R = R_*$. This inner boundary condition is valid when the flow is subsonic. In the supersonic case there is standoff shock, but it requires a separate investigation. From the other side, these boundary conditions are valid for any of these cases if the boundary is not the surface of the star but corresponds to some intermediate layers of the magnetosphere, while the real surface of the star is at smaller radii. Thus, the obtained parameters of the hot spots reflect the distribution of these parameters in the cross section of the funnel streams.

At the outer boundary $R = R_{\max}$, free boundary conditions are taken for all variables. We investigated different types of boundary conditions for the magnetic field but did not observe a significant difference because the magnetic field of the dipole decreases very rapidly with distance and the difference is much less dramatic compared with that of a monopole magnetic field (Ustyugova et al. 1999). We also investigated the possible influence of the outer boundary conditions by running cases in which $R_{\max}/R_* = 14, 40$, and 194. We found the same

results except for the case $R_{\max}/R_* = 14$, in which the accretion rate decreases too fast because the reservoir of matter in the disk is too small. Results for the medium and large regions are very close, so that we took $R_{\max}/R_* = 40$ as the standard size of the simulation region.

2.2. Dimensionless Variables and Reference Values

We use the following dimensionless variables: the length scale $r' = r/R_0$, the fluid velocity $\mathbf{v}' = \mathbf{v}/v_0$, the density $\rho' = \rho/\rho_0$, the magnetic field $B' = B/B_0$, the pressure $p' = p/p_0$, the temperature $T' = T/T_0$, and time $t' = t/t_0$. The variables with zero subscripts are dimensional reference values, which are different for different objects.

The reference values are determined as follows: the unit of distance R_0 is taken to be the initial inner radius of the disk, $R_0 = (R_d)_{t=0}$, so that $r' = 1$ at this radius. The star has radius $R_* = 0.35R_0$. The reference velocity is the Keplerian velocity at R_0 , $v_0 = (GM/R_0)^{1/2}$, and $\omega_0 = v_0/R_0$ is the angular velocity. The reference time is $t_0 = R_0/v_0$. However, in discussing our results we measure time in units of the Keplerian period of the disk, $P_0 = 2\pi t_0$. The reference magnetic field, B_0 , is the initial magnetic field strength at $r = R_0$. The reference density is taken to be $\rho_0 = B_0^2/v_0^2$. The reference pressure is $p_0 = \rho_0 v_0^2$. The reference temperature is $T_0 = p_0/\mathcal{R}\rho = v_0^2/\mathcal{R}$, where \mathcal{R} is the gas constant. The reference accretion rate is $\dot{M}_0 = \rho_0 v_0 R_0^2$. The reference energy flux is $\dot{E}_0 = \rho_0 v_0^3 R_0^2$. The reference value for the blackbody temperature of the hot spots is $(T_{\text{eff}})_0 = (\rho_0 v_0^2/\sigma)^{1/4}$, where σ is the Stefan-Boltzmann constant.

Subsequently, we drop the primes on the dimensionless variables and show dimensionless values in most of the figures. Two types of initial conditions for the disk in dimensionless variables are considered: $\rho_d = 1$, $\rho_c = 0.03$, $T_d = 0.03$, and $T_c = 1$ for the warmer disk and $\rho_d = 1$, $\rho_c = 0.01$, $T_d = 0.01$, and $T_c = 1$ for the cooler disk. Below, we discuss dimensional examples for stars with relatively small magnetospheres, CTTSs, and millisecond pulsars.

2.3. Reference Values for Classical T Tauri Stars

Here we discuss the numerical parameters for a typical CTTS. We take the mass of the star to be $M_* = 0.8 M_\odot$, and its radius, $R_* = 1.8 R_\odot$. The magnetic field at the surface of the star is assumed to be $B_* = 10^3$ G. The reference value of length is $R_0 = (1/0.35)R_* \approx 2.86R_* \approx 3.6 \times 10^{11}$ cm. The size of the simulation region corresponds to $R_{\max} \approx 40R_* \approx 0.34$ AU. The reference velocity is $v_0 \approx 1.9 \times 10^7$ cm s $^{-1}$. The period of Keplerian rotation of the inner radius of the disk is $P_0 \approx 1.38$ days. We consider that the star rotates relatively slowly, $P_* = 9.4$ days, which corresponds to many CTTSs. Simulations for higher rotational velocities did not bring substantially new results (excluding the propeller stage, of course, which we do not discuss here). The reference magnetic field is $B_0 = B_*(R_*/R_0)^3 \approx 42.7$ G. The reference density is $\rho_0 = 4.9 \times 10^{-12}$ g cm $^{-3}$, or $n = 3.06 \times 10^{12}$ cm $^{-3}$, which is typical for T Tauri star disks (see, e.g., Hartmann 1998). The reference temperature is $T_0 = 4.5 \times 10^6$ K, which corresponds to a typical temperature in the corona and to the temperature $T_d = 4.5 \times 10^4$ K in the innermost part of the disk for a run typical for CTTSs ($T_d = 0.01$ and $T_c = 1$). The reference mass accretion rate is $\dot{M}_0 \approx 1.2 \times 10^{19}$ g s $^{-1} \approx 1.9 \times 10^{-7} M_\odot$ yr $^{-1}$. The reference value for the energy flux is $\dot{E}_0 \approx 4.5 \times 10^{33}$ ergs s $^{-1}$, and for the blackbody temperature it is $(T_{\text{eff}})_0 = 5.0 \times 10^3$ K. The dimensionless values of the intensity in Figures 7–9 are $J \approx 2 \times 10^{-3}$ to 1.7×10^{-2} , which corresponds to the dimensional values $J\dot{E}_0 \approx 9.0 \times 10^{30}$ to 7.6×10^{31} ergs s $^{-1}$.

2.4. Reference Values for Millisecond Pulsars

We take the mass of the neutron star to be $M_* = 1.4 M_\odot = 2.8 \times 10^{33}$ g, its radius $R_* = 10$ km = 10^6 cm, and the surface magnetic field $B = 10^8$ G. The reference length scale is $R_0 \approx 2.86R_* = 2.86 \times 10^6$ cm. The reference velocity is $v_0 = 8.1 \times 10^9$ cm s $^{-1}$. The reference period is $P_0 = 2.2 \times 10^{-3}$ s. In application to millisecond pulsars the frequency is often analyzed. The reference frequency is $\nu_0 = 1/P_0 \approx 454$ Hz. The reference magnetic field is $B_0 = B_*(R_*/R_0)^3 \approx 4.3 \times 10^6$ G. The reference density is $\rho_0 = 2.8 \times 10^{-7}$ g $^{-3}$. The reference temperature is $T_0 = 7.8 \times 10^{11}$ K. The reference mass accretion rate is $\dot{M}_0 \approx 1.85 \times 10^{16}$ g s $^{-1} \approx 2.9 \times 10^{-10} M_\odot$ yr $^{-1}$. The reference value for the energy flux is $\dot{E}_0 \approx 1.2 \times 10^{36}$ ergs s $^{-1}$. The reference blackbody temperature is $(T_{\text{eff}})_0 = 4.0 \times 10^6$ K. The dimensionless values of the intensity in Figures 7–9 are $J \approx 2 \times 10^{-3}$ to 1.7×10^{-2} , which corresponds to the dimensional value $J\dot{E}_0 \approx 2.4 \times 10^{33}$ to 2.0×10^{34} ergs s $^{-1}$.

3. PHYSICAL PROPERTIES OF THE HOT SPOTS

In this section we discuss the connection between the shape of the funnel streams and those of the hot spots (§ 3.1), properties of matter along the funnel streams (§ 3.2), and properties of the hot spots (§ 3.3)

3.1. Funnel Streams versus Hot Spots

The shape and other properties of the hot spots are determined by those in the cross section of the incoming funnel stream. R03 observed that the shapes of the funnel streams are different for different misalignment angles, Θ , and may be complicated. At small misalignment angles, $\Theta \lesssim 30^\circ$, matter typically accretes in two streams. For medium angles, $30^\circ \lesssim \Theta \lesssim 60^\circ$, the streams often split into several streams. At larger angles, $\Theta \gtrsim 60^\circ$, matter again accretes in two streams, but they have different shapes compared with those at small Θ . The streams tend to settle close to the μ - Ω plane after a few rotation periods, P_0 . They settle faster for cooler disks and large Θ . We chose one moment of time, $t = 5P_0$, at which many streams settled, and investigated spots in detail for this time.

Figure 1 shows the funnel streams and corresponding hot spots at the surface of the star at time $t = 5P_0$. Only a small part of the simulation region is shown to resolve the inner regions of the funnel streams in greater detail. To show the shape of the funnel streams, we have chosen for each plot a fixed density level that is slightly different for different Θ and varies between $\rho = 0.35$ and 0.45 for smaller Θ (green) and between $\rho = 0.6$ and 0.7 for larger Θ (yellow-green). At these density levels the size of the spots is relatively large, and they occupy approximately 20% of the star's surface area. One can see that at all Θ the density of the spots increases toward their central regions. These results correspond to simulations of a warmer disk, $T_d = 0.03$.

Figure 2 shows similar results but for the cooler disk, $T_d = 0.01$. One can see that the funnel streams and the spots are somewhat similar. However, in this case (which is taken also for the time $t = 5P_0$) the streams and spots are located much closer to their “final,” quasi-equilibrium position (downstream of the μ - Ω plane for a slowly rotating star; R03), compared with those of the warmer disk. For both warmer and cooler disks the spots continue to wander around this quasi-equilibrium position. However, for cooler disks the amplitude of these oscillations is much smaller.

We calculated the filling factor of the spots f (the fraction of the star covered by the spots) for both cases at different

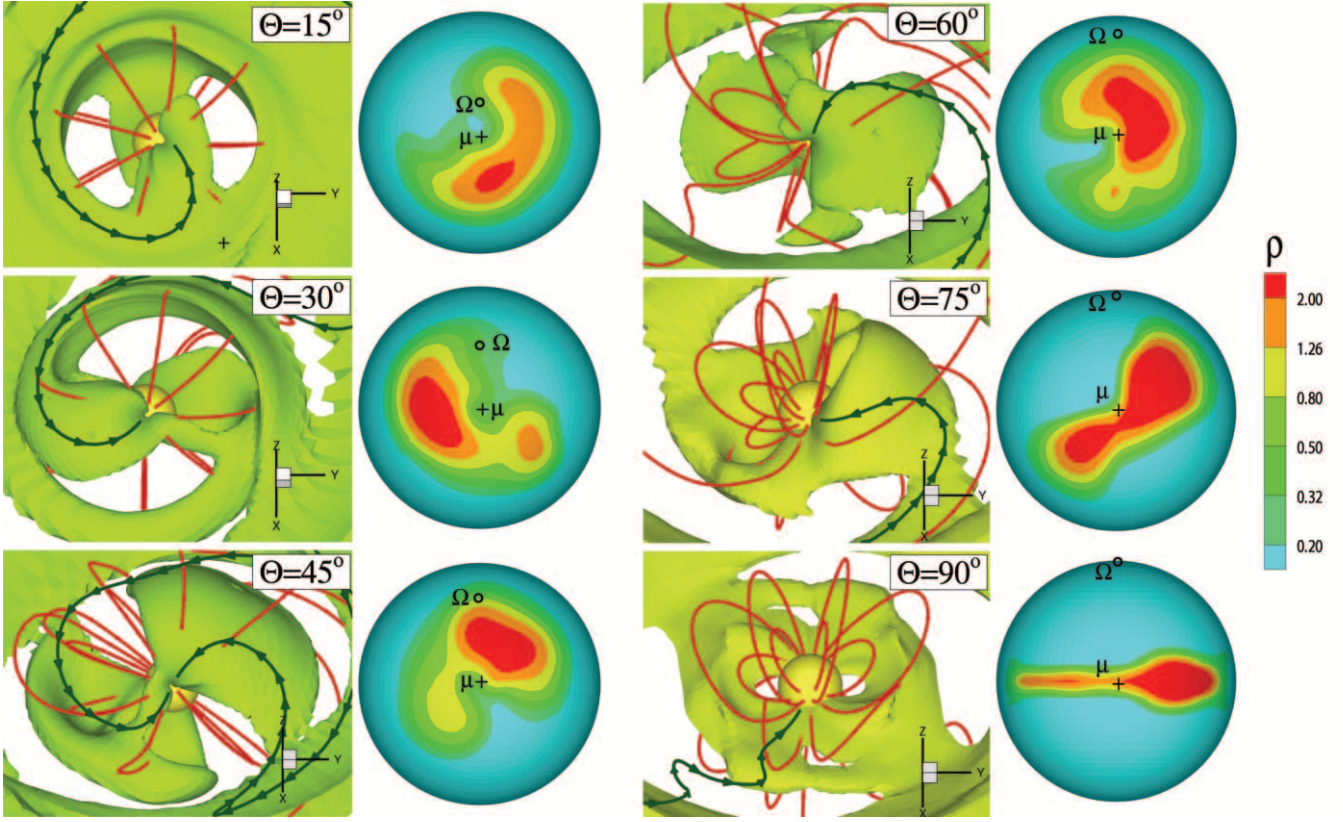


FIG. 1.—Matter flow near the star and hot spots for a relatively warm disk ($T_d = 0.03$). *Square panels*: Surfaces of the density in the magnetospheric flows (green: $\rho = 0.3 - 0.4$; yellow-green: $\rho = 0.6$). Red lines are sample magnetic field lines; the dark green lines show the sample streamlines of matter flow. *Circular panels*: Density distributions in the hot spots for different misalignment angles, Θ . For $\Theta = 15^\circ, 30^\circ$, and 45° , the magnetic axis (crosses) is directed toward the observer, while for $\Theta = 60^\circ, 75^\circ$, and 90° , it is directed at an angle 45° relative to the observer. The direction of the rotation axis is shown with the open circles.

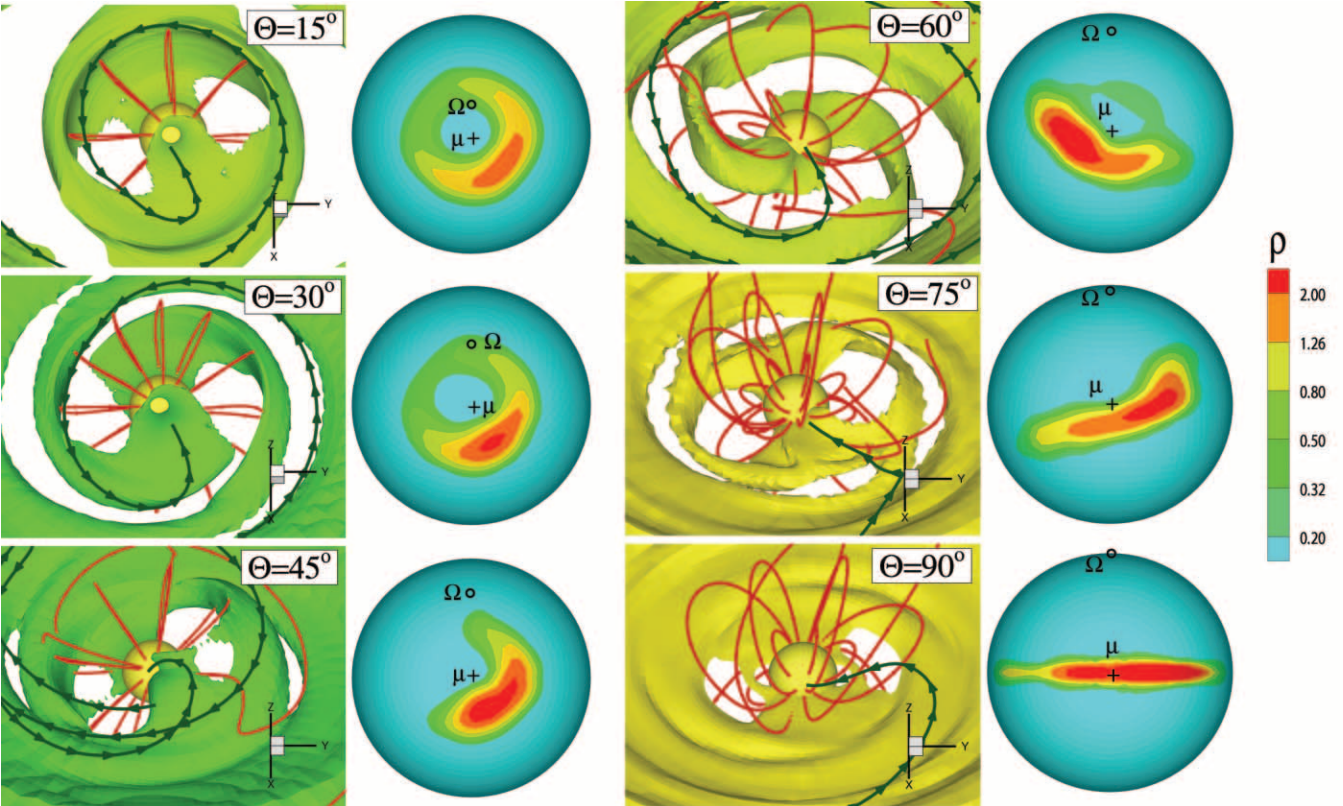


FIG. 2.—Same as Fig. 1, but for a cooler disk ($T_d = 0.01$).

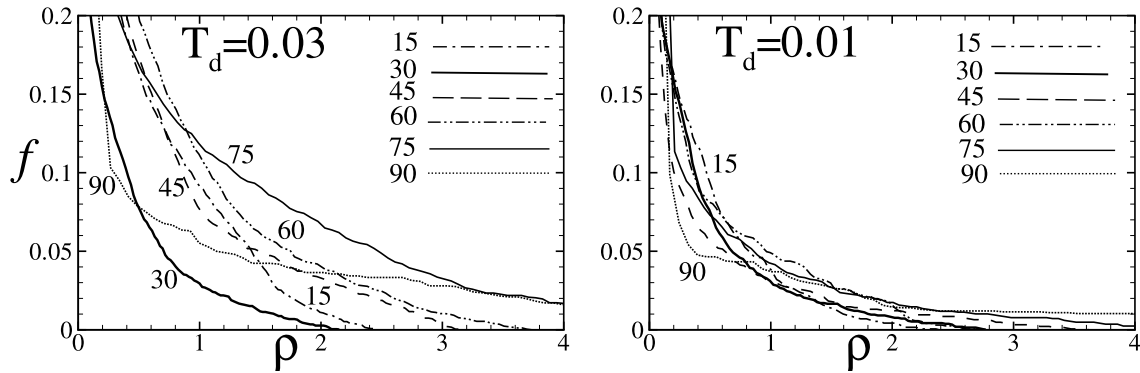


FIG. 3.—Fraction of the star's surface area f covered by the hot spots with density larger than ρ for different misalignment angles, Θ . *Left*, Warmer disk, $T_d = 0.03$; *right*, cooler disk, $T_d = 0.01$.

density levels ρ and different Θ . Figure 3 shows that at a given Θ the value of f decreases with ρ , that is, at larger densities the area covered by the spots is smaller. For warmer disks (Fig. 3, *left*), the size of the spots strongly depends on Θ , especially at larger densities, while for cooler disks, this dependence is much less pronounced. At the density levels corresponding to the funnel streams, the size of the spots is relatively large, and they occupy approximately 10%–20% of the star's surface area. The spots are typically smaller for cooler disks.

3.2. Parameters along the Funnel Stream

To investigate parameters along the funnel stream, we consider the case with $\Theta = 15^\circ$, in which streams have a relatively simple pattern. Figure 4 shows the slice through the middle of the funnel stream for $T_d = 0.03$. One can see that matter accumulates near the magnetosphere, forming a relatively dense region—a ring. When matter goes to the funnel stream, the density along the flow first decreases but later increases because the magnetic field lines converge. Figure 4 shows that the density is largest in the interior regions of the stream and decreases outward to much lower values.

Figure 5 shows velocities along (v_{\parallel}) and across (v_{\perp}) the stream and Mach number $M = v/c_s$, where v is the total velocity. The left panel corresponds to $T_d = 0.03$. One can see that in the beginning of the stream the velocity across the stream, v_{\perp} , is comparable to v_{\parallel} , but it decreases while approaching the star. The velocity does not reach supersonic values because the sound speed is relatively high and also because the pressure gradient decelerates the flow. For a cooler disk (*right*) the v_{\parallel} component is larger, the Mach number is larger than unity, and the flow is supersonic. Below, we investigate the properties of the hot spots for these two cases.

3.3. Density, Velocity, and Matter Flux in the Spots

Figure 6 shows an example of the distribution of different parameters in the hot spots for $\Theta = 30^\circ$ for cases of subsonic flow (*top two rows*) and supersonic flow (*bottom two rows*). One can see that both the density ρ and total velocity v increase toward the central regions of the spot. The distribution of the Mach number $M = v/c_s$ is similar to that of v . The Mach number reaches values $M \gtrsim 2$ in the middle of the spot in the case of the cooler disk.

The matter flux at each point \mathbf{R} of the star's surface is

$$F_M(\mathbf{R}) = \rho \hat{\mathbf{n}} \cdot \mathbf{v}, \quad (1)$$

where $\hat{\mathbf{n}} = -\hat{\mathbf{r}}$ is the inward-pointing normal vector to the star's surface. The total mass accretion rate is

$$\dot{M} = R_*^2 \int d\Omega F_M(\mathbf{R}), \quad (2)$$

where $d\Omega$ is the solid angle element. Figure 6 shows that the F_M distribution is similar to those of density and velocity. Note that in both the subsonic and supersonic cases the maximum values of F_M are approximately the same, which reflects the fact that the accretion rate from the disk is approximately the same in both cases.

3.4. Energy Flux and Temperature in the Spots

Matter flowing to the star in an accretion stream carries both kinetic and thermal energy. The associated energy flux through the surface of the star at the point \mathbf{R} is

$$F_e(\mathbf{R}) = \rho \hat{\mathbf{n}} \cdot \mathbf{v} \left(\frac{1}{2} v^2 + w \right), \quad (3)$$

where \mathbf{v} is the velocity of plasma relative to the surface of the star, $w = \gamma(p/\rho)/(\gamma - 1)$ is the specific enthalpy of the plasma, and $\hat{\mathbf{n}} = -\hat{\mathbf{r}}$ is the inward-pointing normal to the surface of the star.

The detailed physics of the hot spots is complicated. To calculate the spectrum of radiation from the hot spots, an analysis of the radiation transfer is needed (see, e.g., Lamzin 1998; Muzerolle et al. 1998, 2001). This paper does not include an analysis of the radiation transfer. We obtain approximate temperature distributions in the hot spots on the basis of overall energy conservation. Namely, we assume that the energy released in the hot spots is due to the energy flux of equation (3). The region is considered to radiate as a blackbody. Thus, $F_e(\mathbf{R}) = \sigma T_{\text{eff}}^4$, where $\sigma = 5.67 \times 10^{-5}$ ergs $\text{s}^{-1} \text{cm}^{-2} \text{K}^{-4}$ is the Stefan-Boltzmann constant and T_{eff} is the effective blackbody temperature of the radiation. Thus, we get

$$T_{\text{eff}}(\mathbf{R}) = \left[\frac{\rho \hat{\mathbf{n}} \cdot \mathbf{v}}{\sigma} \left(\frac{1}{2} v^2 + w \right) \right]^{1/4}. \quad (4)$$

Figure 6 shows the distribution of F_e and T_{eff} in the spots. Their shapes are similar to that of the density. The distribution

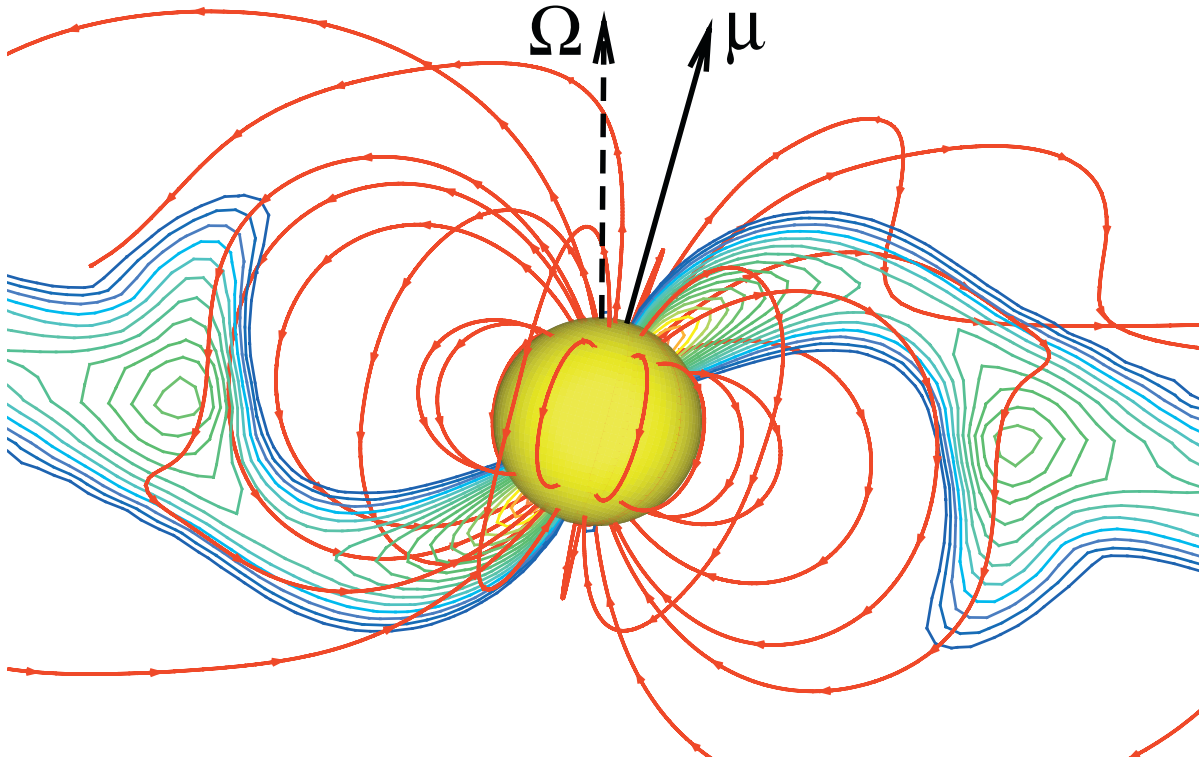


FIG. 4.— X - Z slice through the middle of the funnel stream at $\Theta = 15^\circ$. The contour lines show the plane cross section of the density distribution inside the funnel stream. The density changes exponentially from $\rho = 0.2$ (blue) to $\rho = 2.0$ (red). The density in the corona above the disk is $\rho = 0.01$ – 0.02 . Red lines with arrows show selected magnetic field lines. The magnetic moment, μ , and the rotation axis, Ω , are shown.

of T_{eff} is important for understanding the variability in different spectral bands. The spots are expected to be smaller at higher T_{eff} and larger at lower T_{eff} . An indication of such a distribution may have been observed in the CTTS object BP Tauri, where the estimated area of the hot spots was different when different methods were used. Errico et al. (2001) estimated the area to be 20% of the surface of the star. They used spectral lines that are thought to originate in the external regions of the funnel flow. Ardila & Basri (2000) estimated the area to be much smaller, 0.3%. However, they modeled the UV continuum, which originates in the hottest region of the spots. Note that in the present analysis, we do not take into account the radiation coming from the interior of the star.

4. INTENSITY OF RADIATION AND LIGHT CURVES

To calculate the radiation intensity from the hot spots, we suppose that all the kinetic energy flux $F_e(\mathbf{R})$ goes into radiation. The energy radiated from a unit area of the spot is

$$F_e(\mathbf{R}) = \int_{\cos \theta > 0} d\Omega f(\mathbf{R}, \mathbf{m}), \quad (5)$$

where $f(\mathbf{R}, \mathbf{m})$ is the intensity of the radiation from a unit area into the solid angle element $d\Omega$ in the direction \mathbf{m} with $\mathbf{m} \cdot \hat{\mathbf{r}} = \cos \theta$. The condition $\cos \theta > 0$ corresponds to the upper

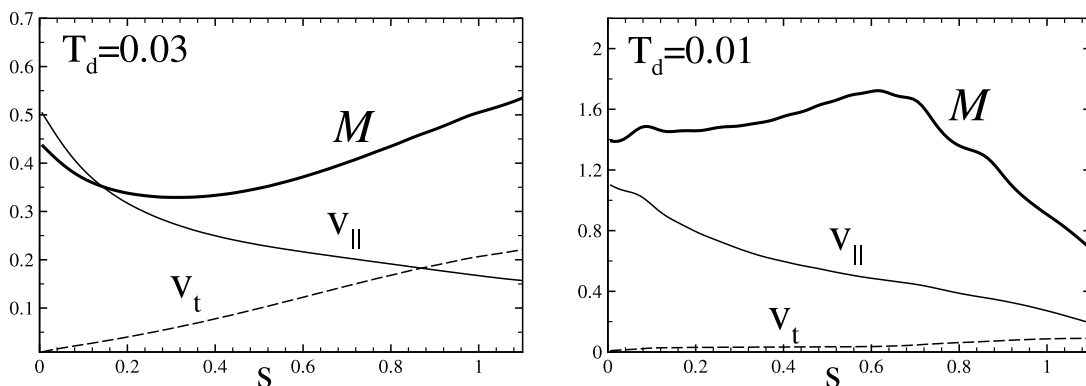


FIG. 5.—Distribution of velocities along a magnetic field line passing approximately through the middle of the funnel stream, obtained at $\Theta = 15^\circ$. The variable s is the linear distance along this magnetic field line, with $s = 0$ at the surface of the star. Here v_{\parallel} is the velocity along the field line, v_t is the velocity in the perpendicular direction, and $M = v/c_s$ is the Mach number based on the total velocity of the flow. *Left*, subsonic flow; *right*, supersonic flow.

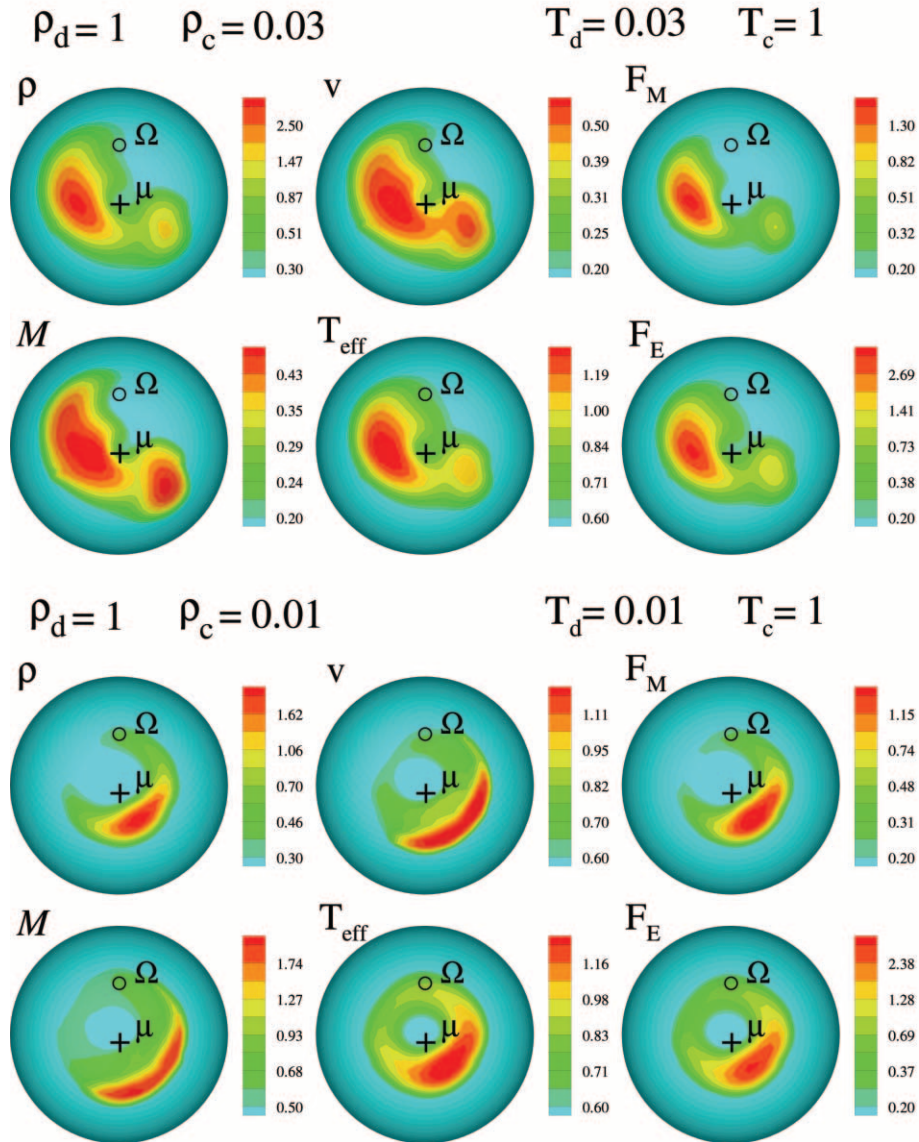


FIG. 6.—Distribution of different physical parameters in the hot spots for the misalignment angle $\Theta = 30^\circ$ and for two types of initial conditions in the disk and corona. The symbol ρ is the density, v is the total velocity, T_{eff} is the effective temperature, M is the Mach number of the flow, and F_M and F_E are the fluxes of mass and energy, respectively. *Top two rows*, Higher temperature in the disk and subsonic flow; *bottom two rows*, lower temperature in the disk and supersonic flow.

half-space above the star's surface. For specificity we consider $f(\mathbf{R}, \mathbf{m}) = A(\mathbf{R}) \cos \theta$. Thus, we obtain the luminosity per unit area at point \mathbf{R} ,

$$F_E(\mathbf{R}) = 2\pi A(\mathbf{R}) \int_0^{\pi/2} \sin \theta \cos \theta d\theta = \pi A(\mathbf{R}), \quad (6)$$

and the intensity of the radiation from a unit area,

$$f(\mathbf{R}, \mathbf{m}) = \frac{1}{\pi} F_E(\mathbf{R}) \cos \theta. \quad (7)$$

Consider now the intensity of radiation seen by a distant observer. The unit vector from the star to the observer is denoted $\hat{\mathbf{k}}$. This vector makes an angle β with the normal to the star's surface; that is, $\cos \beta = \hat{\mathbf{k}} \cdot \hat{\mathbf{r}}$. The intensity of radiation

in the direction $\hat{\mathbf{k}}$ is obtained by integrating over the stellar surface,

$$J = \int dS f(\mathbf{R}, \hat{\mathbf{k}}) = \frac{1}{\pi} \int_{\cos \beta > 0} dS F_E(\mathbf{R}) \cos \beta, \quad (8)$$

where dS is an element of the surface area of the star. In the condition $\cos \beta > 0$, or $\beta < \pi/2$, only the near side of the star is visible. The rotation of a star with hot spots leads to variations in the observed emission J .

4.1. Variability Curves for Fixed Positions of Spots

Hot spots constantly change their shape and position. However, in many situations the changes are small (e.g., a cooler disk), so that as a first step we suppose that the spots have a fixed location at the surface of the star and that this

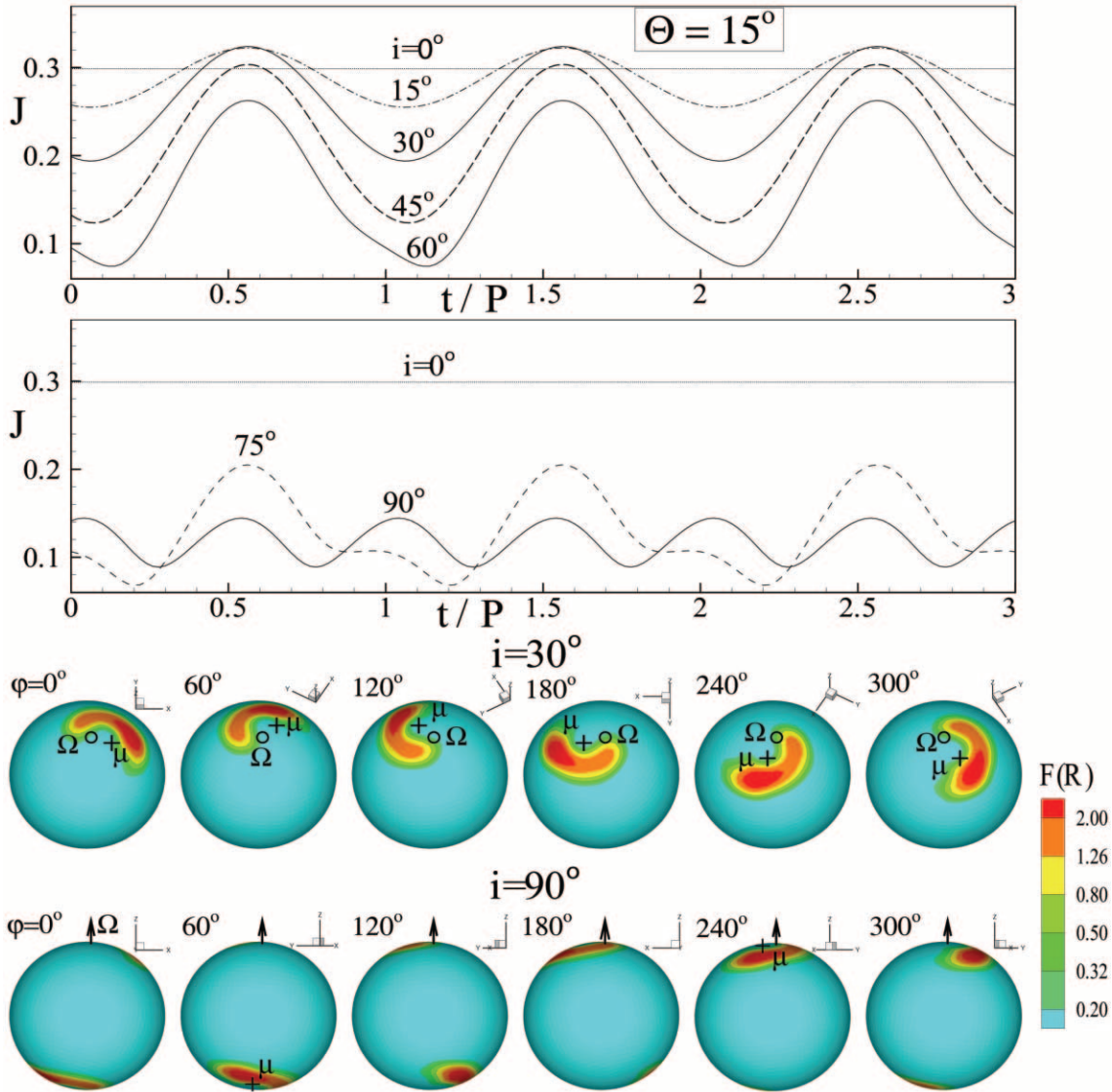


FIG. 7.—Light curves calculated for the small misalignment angle $\Theta = 15^\circ$ and for different inclination angles, i . Time, t , is measured in periods of rotation of the star, P . Two bottom rows: Distribution of energy flux $F(R)$ in the hot spots at different phases, φ , of the star seen by an observer at inclination angles $i = 30^\circ$ and 90° . Phases are shown for one period of rotation. The magnetic and rotation axes are marked with a circle and a cross, respectively.

variability is connected to the rotation of the star relative to the fixed observer. This approach helps to explain different features of the light curves that are associated with structure and location of the hot spots at different Θ . Examples of actual variability curves are shown in § 4.2.

We consider one of the initial conditions (warmer disk, $T_d = 0.03$), take hot spots at a single moment of time, $t = 5P_0$ (as in Fig. 1), and calculate from equation (8) the observed intensity, $J(t)$, as the star rotates. Such light curves were calculated for the misalignment angles $\Theta = 15^\circ, 45^\circ$, and 75° and for different inclination angles of the disk, i , with respect to the line of sight. The inclination angle of the disk is the angle between the direction of Ω and the direction to the observer, \hat{k} . That is, $\cos i = \Omega \cdot \hat{k}$. The results are shown in Figures 7–9.

Figure 7 shows results for a relatively small misalignment angle $\Theta = 15^\circ$. Figure 7 (top) shows the light curves for different inclination angles, i . Figure 7 (bottom) shows the orientation of the star during one rotation period. The phases are

shown for two cases: at $i = 30^\circ$, which is a probable inclination angle, and at $i = 90^\circ$, which is edge-on.

Of course for $i = 0^\circ$ there is no variability because the observer sees only one hot spot, which rotates around the Ω -axis. For larger inclination angles, such as $i = 15^\circ, i = 30^\circ, i = 45^\circ$, dips that increase with increasing values of i appear in the light curves. These dips are connected to the fact that the hot spots come closer to the edge of the star and are partially obscured. Under these conditions the star is observed as a variable star with one maximum per period. For $i = 60^\circ$, the light curve becomes asymmetric, and this asymmetry increases for larger inclination angles, i . This is connected to the fact that the second spot, which was invisible at smaller i , appears and starts to contribute to the luminosity. Thus, two intensity maxima per stellar period are observed. The two maxima become equal in amplitude at $i = 90^\circ$.

Figure 8 shows similar plots but for the misalignment angle $\Theta = 45^\circ$. The light curves in this case are similar to those at

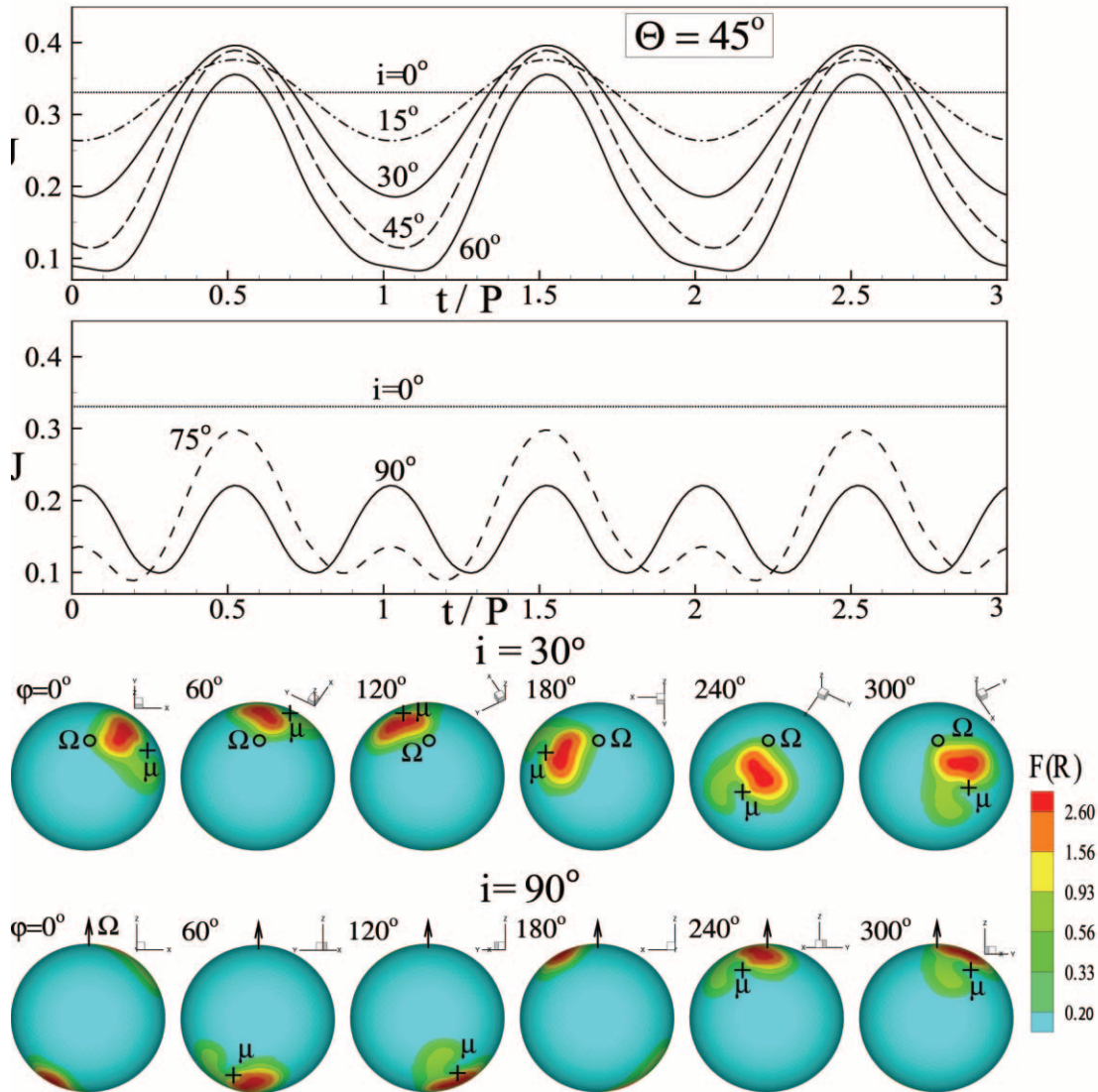


FIG. 8.—Same as Fig. 7, but for a medium misalignment angle, $\Theta = 45^\circ$.

smaller Θ . However, the shorter timescale variability appears at large inclination angles, $i \gtrsim 75^\circ$. Figure 9 shows the case of a high misalignment angle, $\Theta = 75^\circ$. For this and larger values of Θ , the double-maxima (half-period) variability appears for many inclination angles starting from $i \gtrsim 30^\circ$.

Figures 7–9 show intensity in dimensionless units. This value in dimensional units is $J\dot{E}_0$, where \dot{E}_0 is the dimensional energy flux (see §§ 2.3 and 2.4). The value of $J\dot{E}_0$ gives the energy flux from the spots that radiated in the direction of the observer. This value determines the observed flux when the distance to the object is taken into account. Thus, the X-ray flux observed, e.g., from millisecond pulsars, is proportional to J , and the expected variability curves are similar to those in Figures 7–9. However, for CTTs it is common to show the light curves on a logarithmic scale, using the standard stellar magnitude values. As long as this analysis can be applied to stars at different distances, we accept the random null point for calculating m , which is different for different CTTs. We suppose that the intensity $J = 0.1$ corresponds to $m = 12$ and calculate the light curve using the standard formula $m = 12 -$

$2.512(1 + \log J)$. Figure 10 shows light curves in stellar magnitudes for different Θ and i . Note that the curves have different shapes, which may be used to estimate values of Θ and i .

4.2. Variability Curves for Changing Spots

Here we present samples of actual variability curves. We take the data for all moments of time from the numerical simulations. The star rotates slowly, with $\Omega_* = 0.19$, so that one rotation of the star corresponds to 5.26 rotations of the inner radius of the disk: $P_* \approx 5.3P_0$. Thus, to show the variability pattern during a few rotations of the star, we need pretty long runs. Here we show sample results from several relatively long runs with $t = (15-16)P_0$. Figure 11 shows sample light curves for the cooler disk and $\Theta = 15^\circ$ and 45° . One can see that the “real” light curves have features similar to the curves for fixed hot spots. However, the variability pattern departs from the exact variability patterns shown in Figures 7 and 8. This is because the hot spots continue to change their shape and position. Figure 12 shows variability curves for larger misalignment angles, $\Theta = 75^\circ$ and 90° (for a

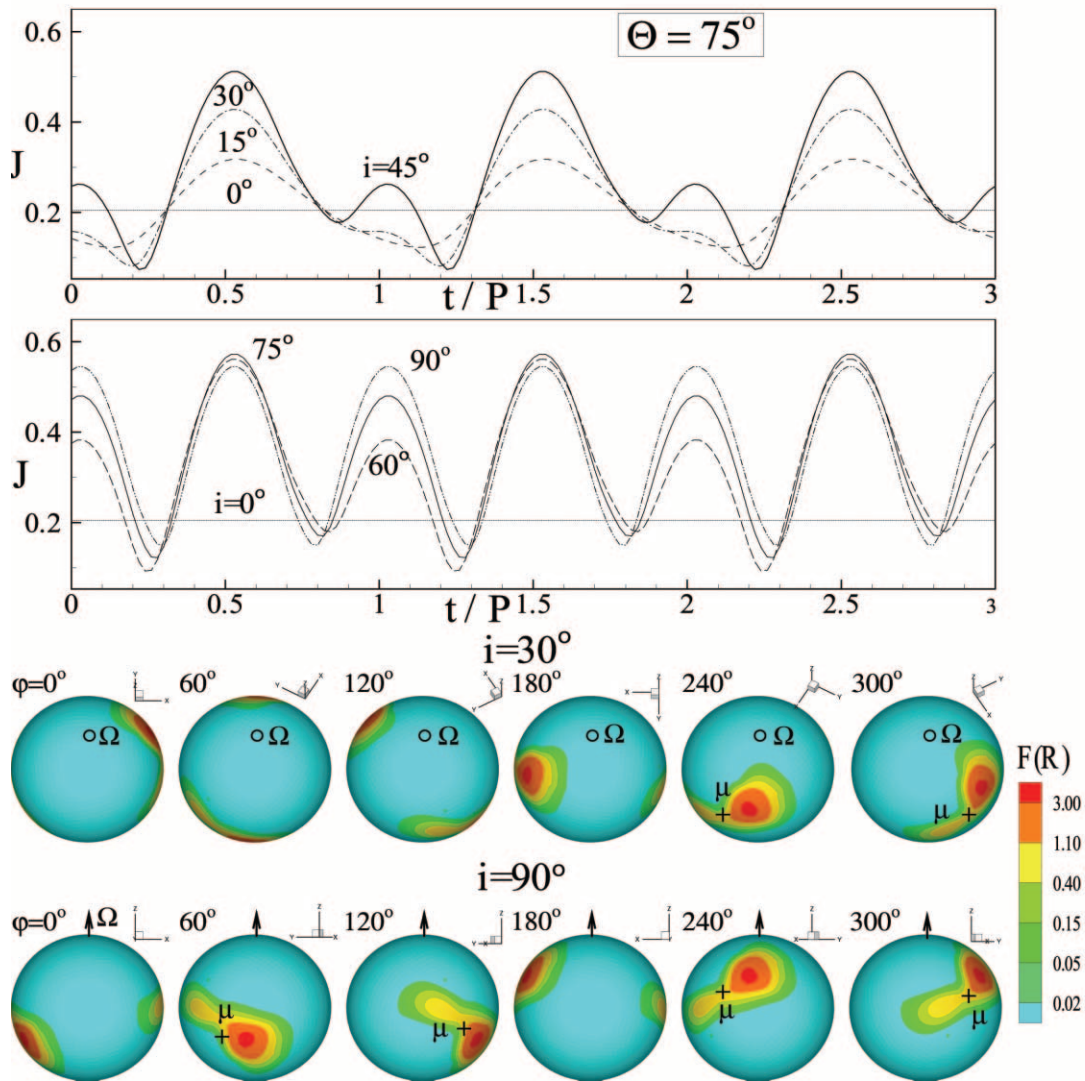


FIG. 9.—Same as Fig. 7, but for a large misalignment angle, $\Theta = 75^\circ$.

warmer disk). One can see that at these misalignment angles the light curves are closer to those of Figure 9 because the spots have almost fixed positions on the stellar surface.

5. DISCUSSION

In this paper we fixed parameters of the star and the flow. Below, we discuss the dependence of the results on Ω_* and on the accretion rate \dot{M} . In § 5.2 we discuss the limitations of the model and future work.

5.1. Dependence of Results on Parameters of the Star and the Disk

Ω dependence.—For the results given here we have taken a relatively low angular velocity, $\Omega_* = 0.19$. This corresponds to CTTSs with a period of $P = 9.4$ days. We did additional simulations for an intermediate angular velocity, $\Omega_* = 0.35$ ($P = 3.3$ days), and a rapidly rotating star, $\Omega_* = 1.0$ ($P = 1.8$ days). We observed that the hot-spot shapes are similar for slowly and rapidly rotating stars. For the intermediate angular velocity, the bow shape is less prominent. The bow shape of the hot spots reflects the typical shape of the funnel streams,

whose thicknesses are small compared with their widths. This is typical for relatively small inclination angles, $\Theta \lesssim 30^\circ$, for which the stream should climb an appreciable distance above the equatorial plane before accreting to the vicinity of the magnetic pole. At small inclination angles, the bow shape is natural because it can be considered part of the narrow cylindrical ring that occurs for $\Theta = 0^\circ$.

\dot{M} dependence.—We studied the dependence of the size of the spots on the accretion rate \dot{M} . We introduced an α -type viscosity analogous to one used by R02 and performed a set of runs at different values of the accretion rate \dot{M} (different α). Figure 13 shows that the fraction f of the star covered by the hot spots increases with the accretion rate for a range of density levels, $\rho = 0.4, 1,$ and 2 . Thus, the size of the spots increases as the accretion rate increases. This is in accord with recent results of Ardila & Basri (2000), who analyzed the UV variability of the CTTS BP Tau and showed significant correlation between the accretion rate and the filling factor of the shocks. In R03 we noted that at a larger accretion rate the streams become wider and cover a larger area of the magnetosphere. This may explain the observed variation in the shapes

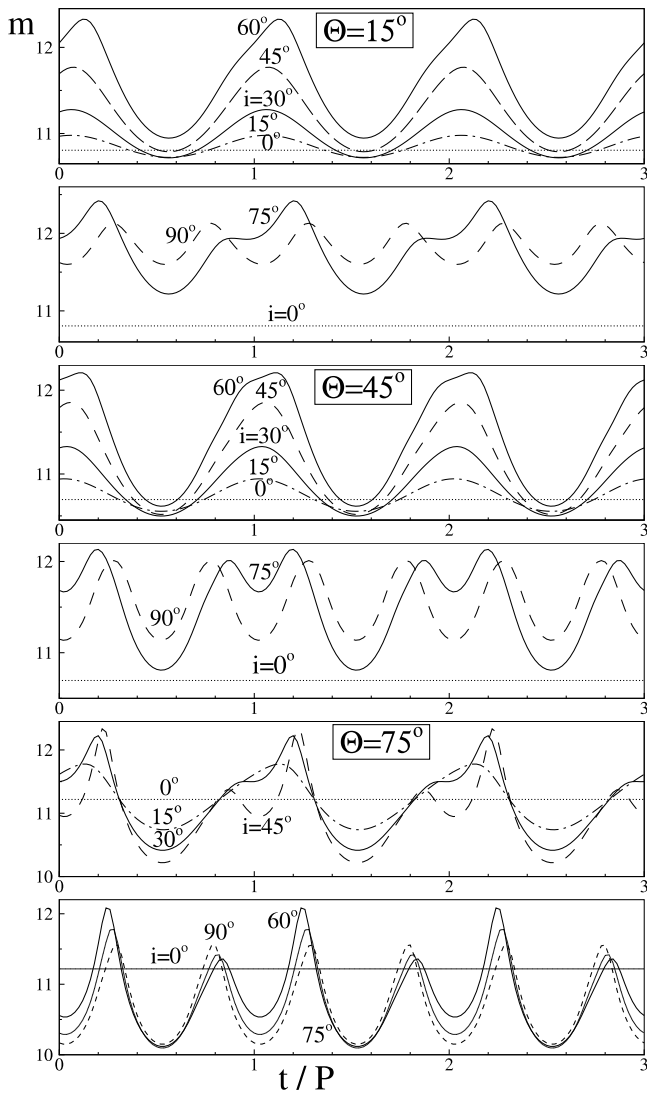


FIG. 10.—Light curves similar to those of Figs. 7–9, but with intensity measured in stellar magnitudes, m . Top two panels, $\Theta = 15^\circ$; middle two panels, $\Theta = 45^\circ$; bottom two panels, $\Theta = 75^\circ$.

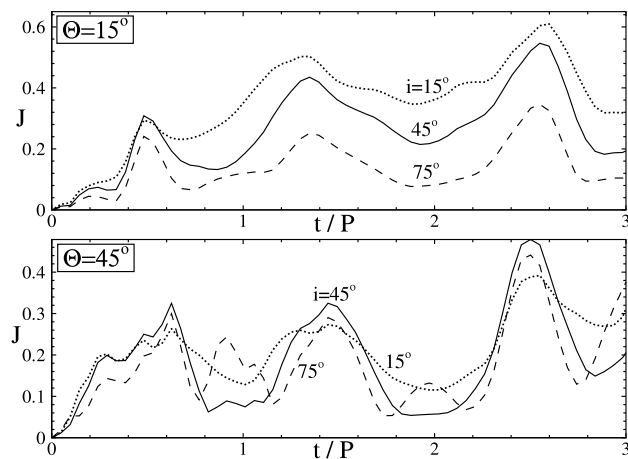


FIG. 11.—Light curves calculated for actual time-dependent hot spots for the misalignment angles $\Theta = 15^\circ$ and 45° and for different inclination angles, i , for the cooler disk, $T_d = 0.01$.

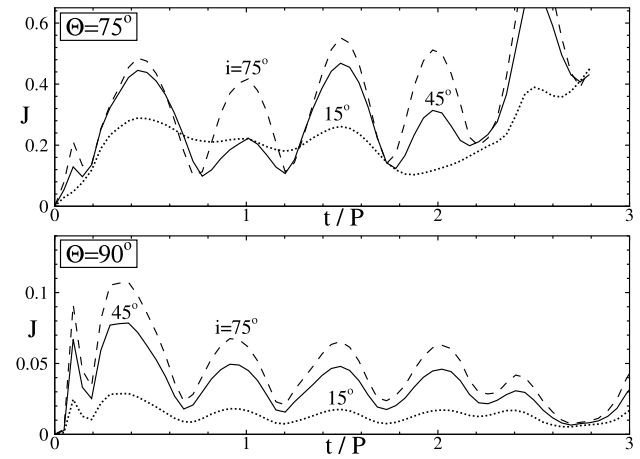


FIG. 12.—Same as Fig. 11, but for misalignment angles $\Theta = 75^\circ$ and 90° for the warmer disk, $T_d = 0.03$.

of the magnetospheric lines with the accretion rate (Muzerolle et al. 2001).

5.2. Limitations of the Model and Future Work

Variability in different spectral lines in the accreting magnetized stars may be associated with different regions: inner regions of the disk, magnetospheric streams, hot spots, and outflows. In this paper we analyze only the variability due to the rotation of the hot spots, while the variability associated with other regions will be investigated in future work. The light from the hot spots may also be obscured by magnetospheric streams or by the warped inner regions of the disk if the star is approximately edge-on (e.g., Bouvier et al. 1999, 2003). This paper does not include the effect of obscuration. The warping of the inner regions of the disk (Aly 1980; Lipunov & Shakura 1980; Lai 1999) was not observed in the simulations, but a special set of simulations will be done for investigation of this possible phenomenon.

The magnetic field of the CTTs or millisecond pulsars may not be a pure dipole field (Safier 1998; Smirnov et al. 2003).

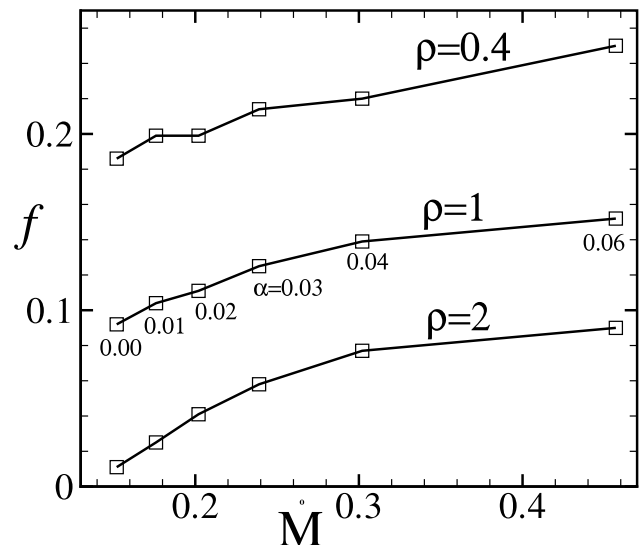


FIG. 13.—Fraction of the star covered by the hot spots at the density levels $\rho = 0.4, 1,$ and 2 as a function of the accretion rate, M . Squares show separate runs at different α -parameters of the disk viscosity.

This can lead to a more complicated geometry of the hot spots and more complicated variability patterns. However, a detailed analysis of the photometric and spectral variability of a number of CCTSs has shown that most of the observed features can be explained by models with a dipole magnetic field (e.g., Muzerolle et al. 1998; Petrov et al. 2001a, 2001b; Alencar et al. 2001; Bouvier et al. 2003). This paper considers only the case in which the star's field is a dipole field. Nondipolar field geometries are investigated separately.

We observed that the hot spots may rotate more rapidly or more slowly than the star, which leads to quasi-periodic oscillations (QPOs) in the light curves and may explain QPOs observed in CTTs (see Smith et al. 1995) and millisecond pulsars (see, e.g., Chakrabarty et al. 2003). QPO variability in disk-magnetized star systems may also be associated with oscillations of the inner radius of the disk (e.g., Goodson et al. 1997). We plan to further investigate the quasi variability associated with such phenomena.

6. SUMMARY

Disk accretion to a rotating star with a misaligned dipole magnetic field has been studied further by three-dimensional MHD simulations. This work focuses on the nature of the hot spots formed on the stellar surface because of the impact of two or more funnel streams. We investigated the shape and intensity of the hot spots for different misalignment angles, Θ , between the star's rotation axis, Ω , and its magnetic moment, μ . Further, we calculated the light curves due to rotation of the hot spots for different angles, i , between the observer's line of sight and Ω . The main results are the following:

1. For small inclination angles, $\Theta < 30^\circ$, the hot spots are typically bow shaped and are bent around the magnetic pole. At large inclination angles, $\Theta \gtrsim 60^\circ$, the shape becomes bar-like. Often a spot on a given hemisphere splits to form two spots, which reflects the splitting of the funnel stream into two streams. The secondary stream is typically weaker than the main stream so that one spot is much larger than the other.

2. The density, temperature, matter flux, and other parameters *increase toward the central regions of the spots*, so that the spots are larger at lower temperature or density and smaller

at larger temperature or density. They cover about 10%–20% of the area of the star at the density level typical for the external regions of the funnel streams (see Figs. 1 and 2). The size of the hot spots increases with the accretion rate.

3. The spots have a tendency to be located close to the μ - Ω plane. They tend to be located downstream of this plane if a star rotates slowly (i.e., the inner region of the disk and the footpoints of the stream rotate somewhat faster than the star) or upstream if a star rotates relatively fast. The spots wander around their “favorite” position. The amplitude of wandering is smaller for a cooler disk.

4. The calculated light curves reveal the following features: (1) The light curve has one peak per one period of rotation of the star, and the shape is approximately sinusoidal. This is typical for small and medium misalignment angles, $\Theta \lesssim 45^\circ$, and inclination angles $i \lesssim 60^\circ$. (2) The light curve has two peaks per period of rotation. This is typical for all Θ if the inclination angle is large, $i > 75^\circ$. At very large misalignment angles, $\Theta \gtrsim 60^\circ$ – 70° , the double-peaked curve is typical for a wide range of inclination angles, $i \gtrsim 30^\circ$.

5. Variation in the shape and location of the spots leads to departure from exact variability and to *quasi variability*. At small misalignment angles, $\Theta < 30^\circ$, the streams (and hot spots) may rotate with a velocity different from that of the star (R03), thus leading to QPOs.

This research was conducted using the resources of the Cornell Theory Center, which receives funding from Cornell University, New York State, federal agencies, foundations, and corporate partners. This work was supported in part by NASA grants NAG5-13220 and NAG5-13060 and by NSF grant AST 03-07817. A. V. K. and G. V. U. were partially supported by grants INTAS CALL2000-491 and RFBR 03-02-16548, by contract MIST 40.022.1.1.1106, and by the Russian astronomy program. The authors thank S. A. Lamzin and P. P. Petrov for discussions about CTTs, D. Chakrabarty and D. Lai for discussions about millisecond pulsars, J. Stinchcombe for editing the manuscript, and the referee for valuable suggestions.

REFERENCES

- Alencar, S. H. P., & Batalha, C. 2002, ApJ, 571, 378
 Alencar, S. H. P., Johns-Krull, C. M., & Basri, G. 2001, AJ, 122, 3335
 Aly, J. J. 1980, A&A, 86, 192
 Ardila, D. R., & Basri, G. 2000, ApJ, 539, 834
 Bildsten, L., et al. 1997, ApJS, 113, 367
 Bouvier, J., & Bertout, C. 1989, A&A, 211, 99
 Bouvier, J., Bertout, C., & Bouchet, P. 1986, A&A, 158, 149
 Bouvier, J., et al. 1993, A&A, 272, 176
 ———. 1999, A&A, 349, 619
 Bouvier, J., et al. 2003, A&A, 409, 169
 Calvet, N., & Gullbring, E. 1998, ApJ, 509, 802
 Camenzind, M. 1990, Rev. Mod. Astron., 3, 234
 Chakrabarty, D., Morgan, E. H., Muno, M. P., Galloway, D. K., Wijnands, R., Van Der Klis, M., & Markwardt, G. B. 2003, Nature, 424, 42
 Errico, L., Lamzin, S. A., & Vittone, A. A. 2001, A&A, 377, 557
 Ghosh, P., & Lamb, F. K. 1979, ApJ, 234, 296
 Goodson, A. P., Winglee, R. M., & Böhm, K.-H. 1997, ApJ, 489, 199
 Gullbring, E., Calvet, N., Muzerolle, J., & Hartmann, L. 2000, ApJ, 544, 927
 Hartmann, L. 1998, Accretion Processes in Star Formation (Cambridge: Cambridge Univ. Press)
 Hartmann, L., Hewett, R., & Calvet, N. 1994, ApJ, 426, 669
 Hayashi, M. R., Shibata, K., & Matsumoto, R. 1996, ApJ, 468, L37
 Herbst, W., & Koret, D. L. 1988, AJ, 96, 1949
 Herbst, W., et al. 1986, ApJ, 310, L71
 Johns, C. M., & Basri, G. 1995, ApJ, 449, 341
 Koldoba, A. V., Romanova, M. M., Ustyugova, G. V., & Lovelace, R. V. E. 2002, ApJ, 576, L53
 Königl, A. 1991, ApJ, 370, L39
 Lai, D. 1999, ApJ, 524, 1030
 Lamzin, S. A. 1998, Astron. Rep., 42, 322
 Lipunov, V. M., & Shakura, N. I. 1980, Soviet Astron. Lett., 6, 14
 Livio, M., & Pringle, J. E. 1992, MNRAS, 259, L23
 Miller, K. A., & Stone, J. M. 1997, ApJ, 489, 890
 Muzerolle, J., Calvet, N., & Hartmann, L. 2001, ApJ, 550, 944
 Muzerolle, J., Hartmann, L., & Calvet, N. 1998, AJ, 116, 455
 Petrov, P. P. 2003, Astrophysics, 46, 506
 Petrov, P. P., Gahm, G. F., Gameiro, J. F., Duemmler, R., Ilyin, I. V., Laakkonen, T., Lago, M. T. V. T., & Tuominen, I. 2001a, A&A, 369, 993
 Petrov, P. P., Pelt, J., & Tuominen, I. 2001b, A&A, 375, 977
 Romanova, M. M., Ustyugova, G. V., Koldoba, A. V., & Lovelace, R. V. E. 2002, ApJ, 578, 420 (R02)
 ———. 2003, ApJ, 595, 1009 (R03)

- Safier, P. N. 1998, *ApJ*, 494, 336
- Shu, F. H., Najita, J., Ostriker, E. C., Wilkin, F., Ruden, S. P., & Lizano, S. 1994, *ApJ*, 429, 781
- Smirnov, D. A., Fabrika, S. N., Lamzin, S. A., & Valyavin, G. G. 2003, *A&A*, 401, 1057
- Smith, K. W., Bonnel, I. A., & Lewis, G. F. 1995, *MNRAS*, 276, 263
- Trümper, J., Kahabka, P., Ögelman, H., Pietsch, W., & Voges, W. 1986, *ApJ*, 300, L63
- Ustyugova, G. V., Koldoba, A. V., Romanova, M. M., Chechetkin, V. M., & Lovelace, R. V. E. 1999, *ApJ*, 516, 221
- Warner, B. 1995, *Cataclysmic Variable Stars* (Cambridge: Cambridge Univ. Press)
- . 2000, *PASP*, 112, 1523
- Wickramasinghe, D. T., Wu, K., & Ferrario, L. 1991, *MNRAS*, 249, 460